Supplementary Material

Limitations

All analyses and interpretations presented in this work are derived from remote sensing data. Although these remote sensing analyses improve our understanding of eruptive processes and allow new concepts to be developed, inherent limitations are associated with each dataset and analysis method.

The presented overflight optical data provide us with high-resolution details of the topography; however, these data are affected by steam emissions and clouds, and observation opportunities were rather sparse. Therefore, additional processes or effects more complicated than those described cannot be ruled out. Moreover, we processed the data without the collection of on-site GCPs and instead relied on the orbital parameters and the georeferencing of Pleiades data. Therefore, a slight shift could persist, such as translation and/or rotation of the derived photogrammetric products, although the results would not be significantly affected.

The SAR data acquired by TSX overcome some difficulties of the optical data, as SAR signals can penetrate clouds, and images were acquired every 11 days. However, other limitations arise; among them, the most important limitation in this study is the geometric distortion effect inherent to radar data, which leads to shadowing, foreshortening, and layover effects and can limit the interpretation of the data. This problem could be solved by geocoding with high-quality DEMs, which were acquired at the same time as the SAR images to match the recorded topographic features. Here, such data were unfortunately not available for the analyzed images; therefore, we found it more beneficial to analyze the data while maintaining radar coordinates by following a stacking approach. Accordingly, the pixel offset calculations have to be interpreted with care, as a constant pixel dimension and displacement conversion is unlikely; in addition, the pixel offsets depend on azimuth and range, where the latter depends on horizontal and vertical displacements. Therefore, we recommend considering these data in more qualitative terms; nevertheless, this approach provides very important additional information about the construction and destruction processes.

The radar shadow method used in this study to estimate the thicknesses of deposits inside the collapse scars suffers from several limitations. A discrete number of thickness measurements can be derived only in areas characterized by a certain topographic configuration (scar walls or other topographic features oriented within +/- 45° of the satellite's direction of travel and having slopes higher than the SAR incidence angle). To estimate the volume of deposits, we divided the total area into subareas and assumed a homogeneous thickness equivalent to the estimated discrete thickness for each subarea. For the areas where the topographic features are completely covered by deposits, the method allows the estimation of only the minimum thickness related to the whole shadow width, thereby excluding the thickness of deposits accumulated above this portion. By comparing the volumes estimated within the two collapse scars by the shadow method (between 16 December 2018 and 26 August 2019) with the more precise volumes derived through photogrammetric measurements on the closest possible dates (between 18 July 2018 and 22 August 2019 with no activity over 18 July – 16 December 2018), we estimated that the radar shadow method underestimates the volume by 17×10^6 m^3 (or 32%).

The MODIS, L8 and S2 satellite thermal datasets allowed us to derive important quantitative and qualitative information on the thermal activity of Shiveluch. However, some satellite-related and methodological limits must be considered. i) The cloud coverage, especially in regions such as Kamchatka characterized by severe meteorological conditions, represents an important limitation due to the masking of hotspots. ii) The S2 and L8 combined revisit frequency means one image every 2-3 days, which is a good compromise for the field of infrared satellite sensing (Coppola et al., 2020). Nonetheless, for an explosive volcano such as Shiveluch that exhibits rapid and short-lived volcanic events, this temporal resolution is suboptimal and might mean an undersampling of thermal phenomena. iii) A spatial resolution of 20-30 m is sufficient to identify major thermal features in space (i.e., Figure 10 and Supplementary Figures 5 and 6) but does not allow a detailed analysis of small, hot emitting sources or permit very accurate dimensional measurements. iv) For both S2 and L8, SWIR analysis detects only the parts of thermal features with a threshold temperature hotter than approximately 200°C (Massimetti et al., 2020), while all cooler thermal emissions are lost. v) S2 MSI and L8 OLI data are daytime

images, and thus, the analysis of SWIR reflectances could partially include solar reflection effects, possibly leading to a minor but nevertheless present enhancement of nonvolcanic thermal features.

Furthermore, aerial thermal data are also subject to limitations often found in the surveying of active volcanoes with infrared cameras. Each flight was conducted using a different thermal camera, as well as a different acquisition geometry and height (nadir+oblique for the first survey and nadir only for the second). Thus, some uncertainty remains in a direct comparison between the two surveys with actual temperatures. Additionally, both datasets were acquired during the daytime, likely introducing significant artifacts and temperature drifts due to solar heating of the surface rocks. Finally, the low pixel resolution may cause local maximum temperatures to be significantly underestimated if the thermal features are smaller than a single pixel, so small fumaroles will likely show a lower temperature. Despite these drawbacks, the locations of and changes in thermal anomalies throughout the dome can be mapped clearly and are distinguishable from potential background errors; however, the absolute temperature values should be interpreted with some caution.

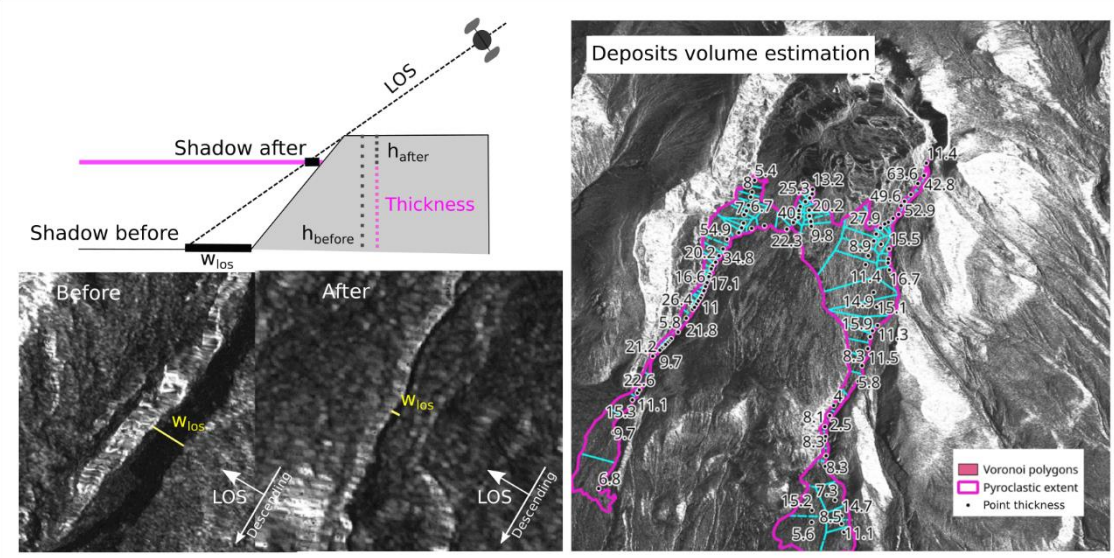

Supplementary Figure 1. Principle of the radar shadow method for estimating the deposit thickness (left) and the method used to estimate the deposit volume (right). Voronoi diagrams based on the point thickness were extracted over the extents of the scars, and the volumes were estimated by multiplying each subarea by the point thicknesses.

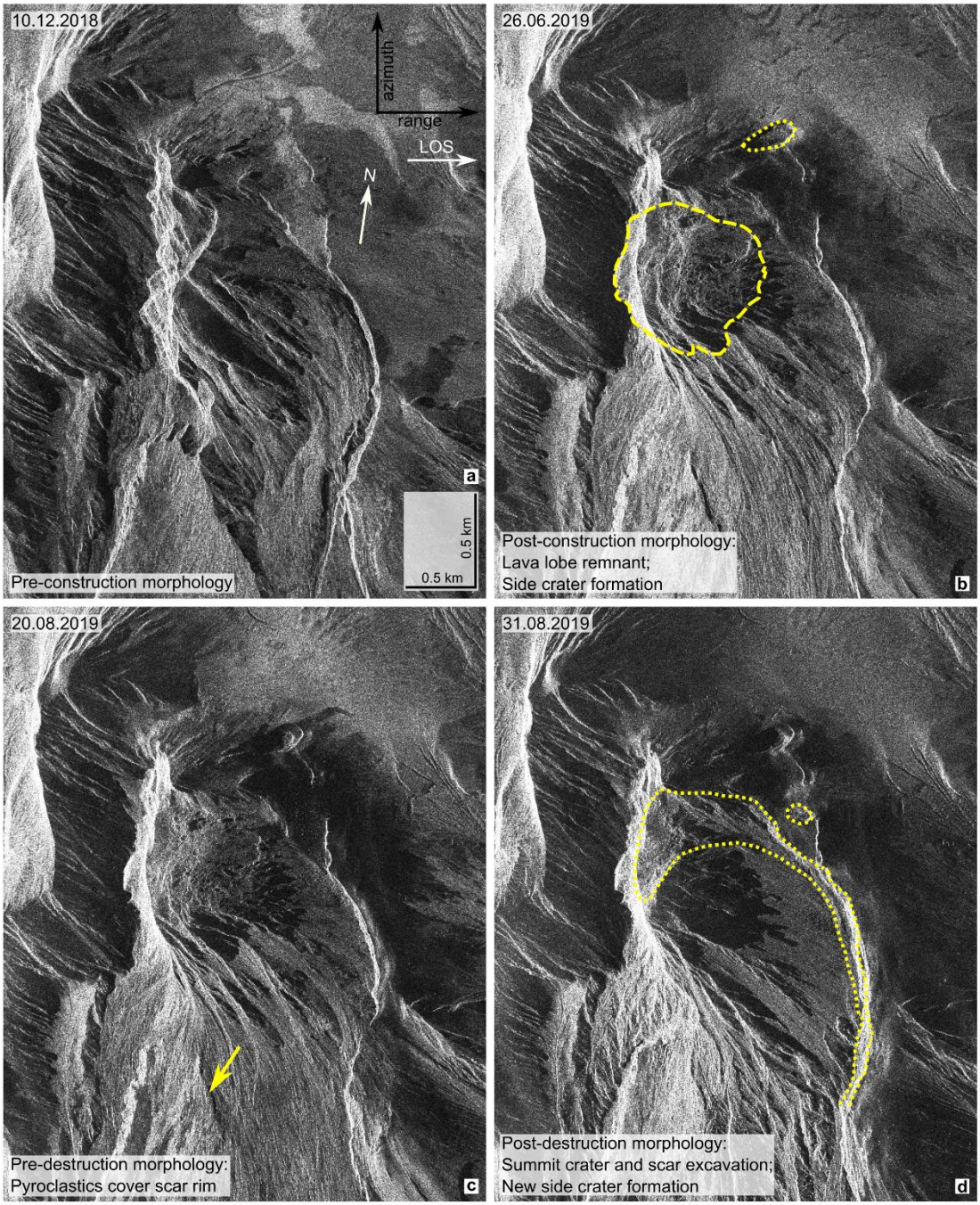

Supplementary Figure 2. Time series of TSX ascending orbit amplitude images (in radar coordinates: azimuth and range) showing the chronology of the eruptive events and main morphological changes that occurred over the studied period. Low-amplitude features (craters and scars) are shown with dotted lines; high-amplitude features (extrusive bodies) are shown with dashed lines. Arrows point to the features labeled in the bottom left corners of the images.

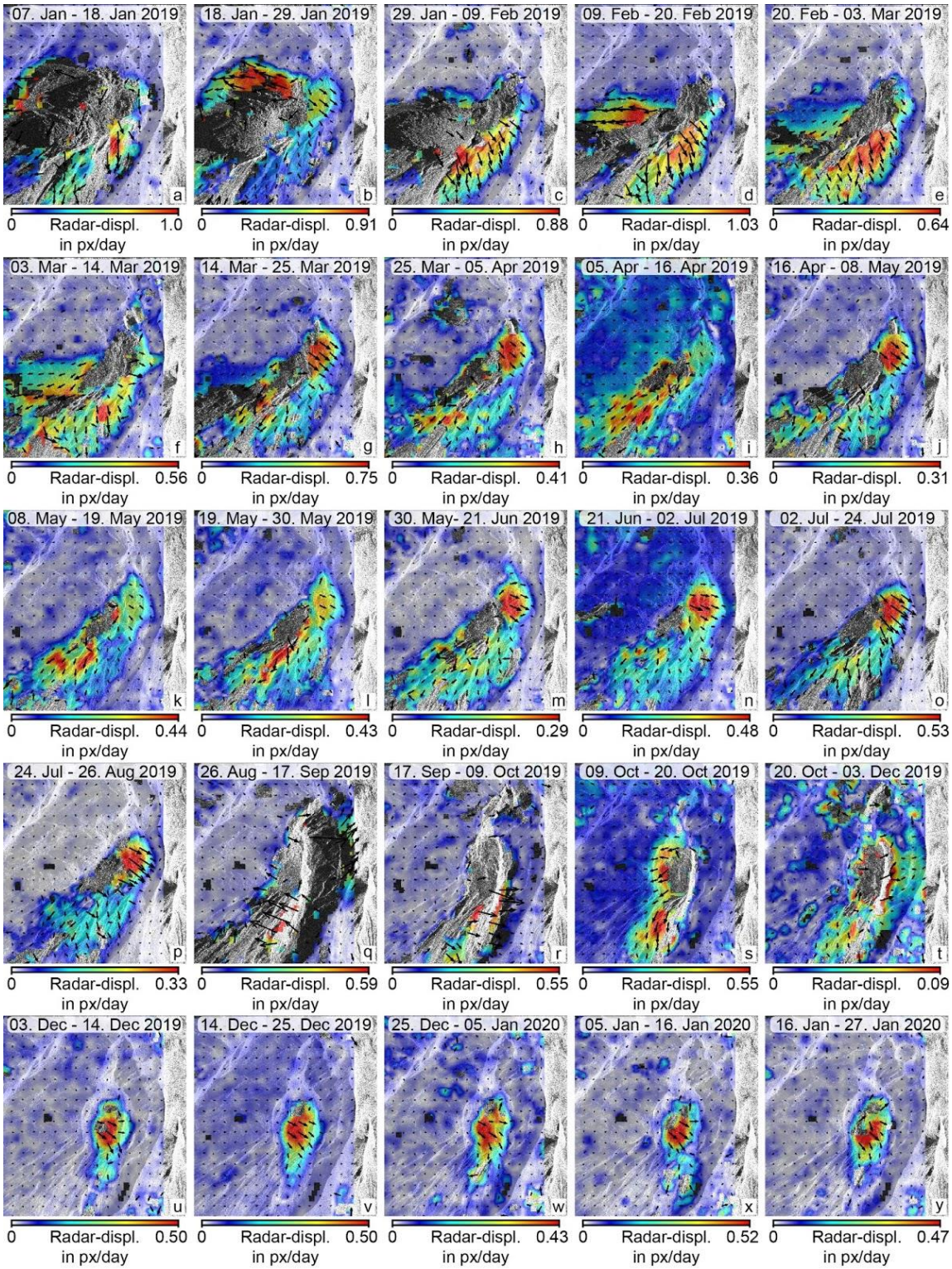

Supplementary Figure 3. PIV tracking maps of surface motions in the radar LOS on the descending view TSX images. The motions show characteristic deformation associated with lava lobe extrusion (a-f), endogenous swelling (g-p), collapse (q-t) and the final stage of endogenous regrowth (u-y).

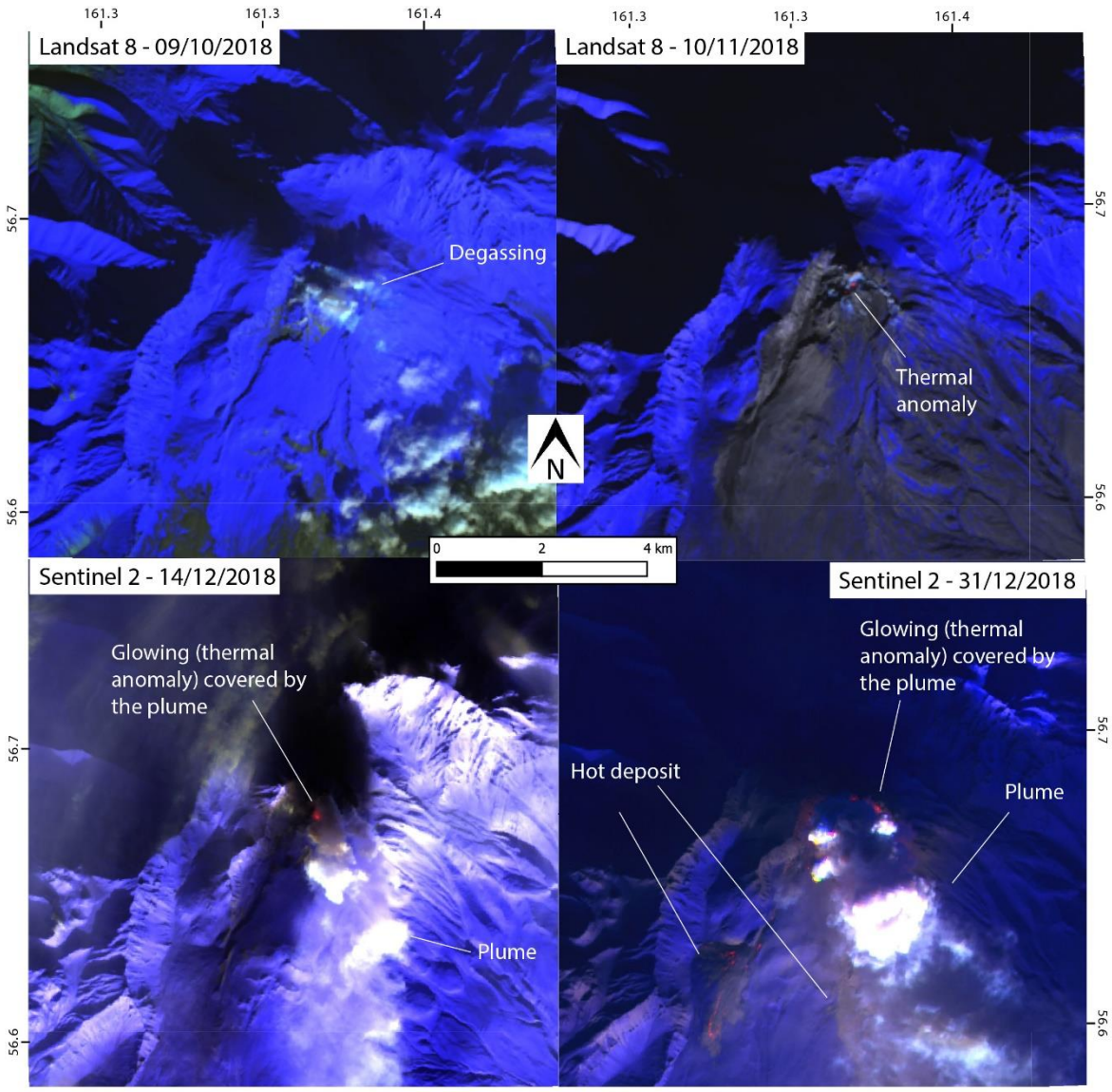

Supplementary Figure 4. S2 MSI and L8 OLI RGB false-color composite in SWIR bands (12-11-8a and 7-6-5, respectively) showing some peculiar events during the evolution of the Shiveluch dome from October 2018 to December 2018. Months before the 30 December 2018 explosion, the dome showed activity consisting of low thermal emissions, degassing, and a plume. The 30 December 2018 explosion caused two pyroclastic flows that extended approximately 5 km from the dome top.

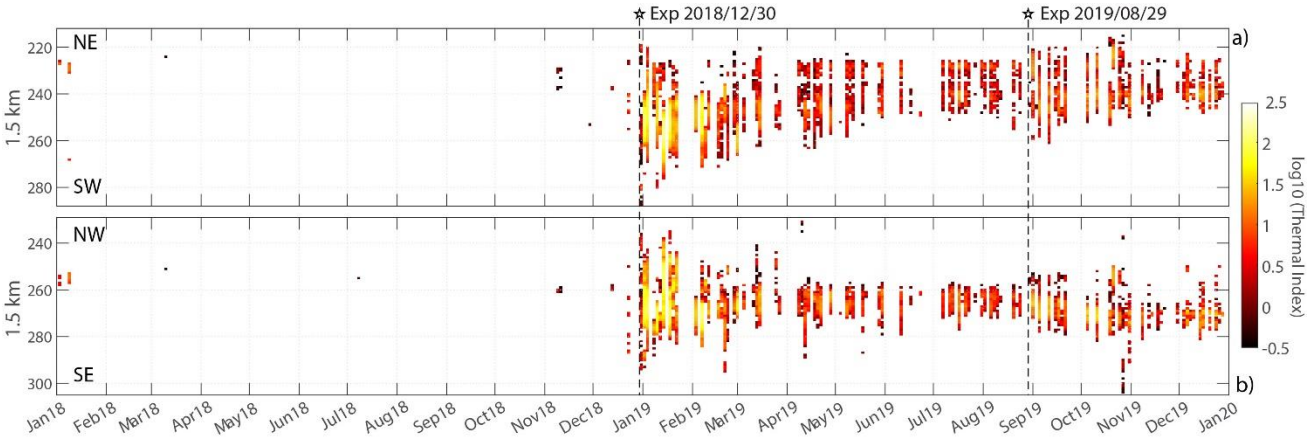

Supplementary Figure 5. Thermal index profiles in the SW-NE (a) and NW-SE (b) directions acquired at the Shiveluch dome (1.5 km width, y-axis in pixels) over the period from January 2018 to December 2020. The thermal index is shown on a logarithmic scale, where darker colors are lower and yellowish-white colors represent high index values. The profiles were produced by stacking S2 and L8 images showing at least one anomalous hot pixel and analyzed in the SWIR bands. The 30 December 2018 and 29 August 2019 events are marked with black stars and dotted lines.

Thermal index profiles

To study the thermal emission anomalies and trends in profile view, we used the S2 and L8 data and constructed thermal emission profiles oriented SW-NE and NW-SE through the Shiveluch dome top. The profiles were generated by stacking the thermal index parameter (Laiolo et al., 2019; Massimetti et al., 2020) in diagonal directions (SW-NE and NW-SE) determined according to the main orientation of the amphitheater axis and the SW-NE lineament identified in this study.

The thermal index parameter was calculated for each pixel detected as "hot" as the sum of the reflectances in the three SWIR bands analyzed herein (e.g., T.I. = ρ12+ ρ11+ ρ8A), which we consider a proxy of the heat source temperature (see Massimetti et al., 2020 for details and Laiolo et al., 2019 for a case study).

The thermal profiles show thermal inactivity throughout 2018 until the first localized hotspots are automatically identified in November 2018 (more precisely, on the L8 and S2 images of 10 and 11 November 2018) one and one-half months prior to the eruption, and these hotspots become increasingly numerous and centralized by December 2018 with some readily identifiable hotspot clusters. Visual examination confirms that these anomalies are real and not related to the background environment, reflections or other nonvolcanic hot emitting sources. These small precursor thermal anomalies are located in the main summit crater atop Shiveluch, particularly on the eastern flank of the summit crater. Following the explosion on 30 December 2018, a thermal zone initially extended towards the southern and SW sectors of the edifice. In March 2019, the explosion strength partially diminished, and we identified anomalies migrating toward the NE and NW. The thermal index magnitude, reflected by the hue intensity from yellow to black, also progressively decreased (dark red tones). From March 2019 to August 2019 (just before the 29 August 2019 explosion), the thermal anomalies appear spatially stable in the SW-NE direction (width of less than 600 m) and show temporary elongation in the SE and SW directions, possibly due mainly to local avalanches. On both profiles, the hotspot locations seem to be spatially constrained by a steady limit towards the NE and NW; in the first case, this constraint is represented by the hotspot located farthest to the NE (Supplementary Figure 5A), while in the second case, this constraint is represented by the abovementioned lineament oriented SW-NE (Supplementary

Figure 5B) that drives the direction of hot material extrusion and deposition. The second main explosion on 29 August 2019 again increased the spatial distribution and intensity of the thermal anomalies. We note the appearance of new hotspots localized towards the NE (Supplementary Figure 5A), indicating the formation of a new active crater to the north in October – November 2019.

Moreover, during this phase, the thermal anomalies moved partially towards the SE, leaving a hotspot-free sector in the center of the dome, where there were stable anomalies until the 29 August 2019 explosion (Supplementary Figure 5B). Then, the thermal activity gradually became more localized and limited to the eastern sector by the end of 2019.

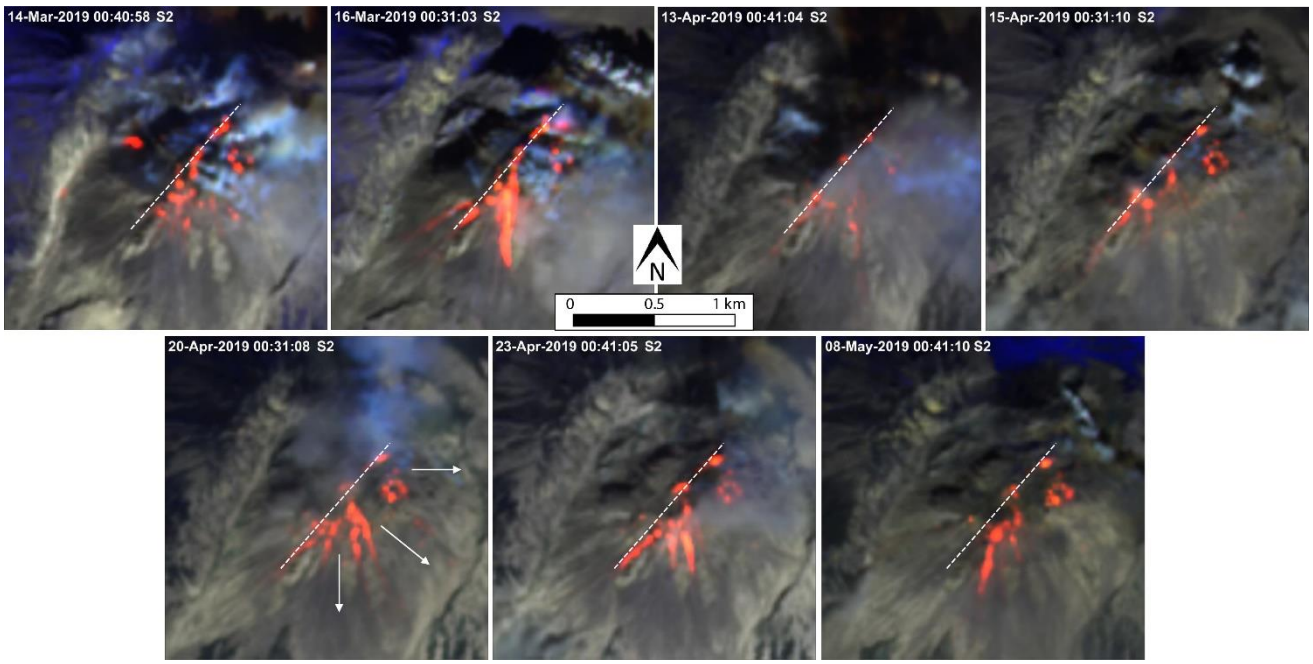

Supplementary Figure 6. Details of the thermal evidence highlighting the NE-SW-trending morphological/structural lineament by S2 MSI false-color composite in SWIR (12-11-8a) band analysis from March 2019 to April 2019. The images are cropped over the Shiveluch dome top within an area of 2 km × 2 km.

Date of survey (dd.mm.yyyy)	Orientation RMSE (m)	Alignment RMSE (m)	Total RMSE (m)	Dome volume error (10^6 m^3)	Dome volume error (%)	Growth rate error (m^3/day)/ (m^3/sec)	Growth rate error (%)
12.07.2012	1.5	2.8	3.2	8.27	1.3	13,824/ 0.16	9.2
18.07.2018	0.2	-	0.2	0.65	0.1	297/ 0.0034	4.1
22.08.2019	1.8	3.1	3.6	12.39	1.6	30,985/ 0.36	8.5
22.10.2019	2	2.3	3.0	10.83	1.6	-	-

Supplementary Table 1. Errors of the photogrammetric model orientation, point cloud alignment, and calculated parameters.

References

Coppola, D., Laiolo, M., Cigolini, C., Massimetti, F., Delle Donne, D., Ripepe, M., et al. (2020). Thermal Remote Sensing for Global Volcano Monitoring: Experiences From the MIROVA System. *Front. Earth Sci.* 7, 362. doi:10.3389/feart.2019.00362

Laiolo, M., Ripepe, M., Cigolini, C., Coppola, D., Della Schiava, M., Genco, R., et al. (2019). Space- and Ground-Based Geophysical Data Tracking of Magma Migration in Shallow Feeding System of Mount Etna Volcano. *Remote Sens.* 11. doi:10.3390/rs11101182

Massimetti, F., Coppola, D., Laiolo, M., Valade, S., Cigolini, C., and Ripepe, M. (2020). Volcanic Hot-Spot Detection Using SENTINEL-2: A Comparison with MODIS–MIROVA Thermal Data Series. *Remote Sens.* 12. doi:10.3390/rs12050820